

# Implicit Regression in Subspace for High-Sensitivity CEST Imaging

## Appendix

### 1 Phantom Simulation

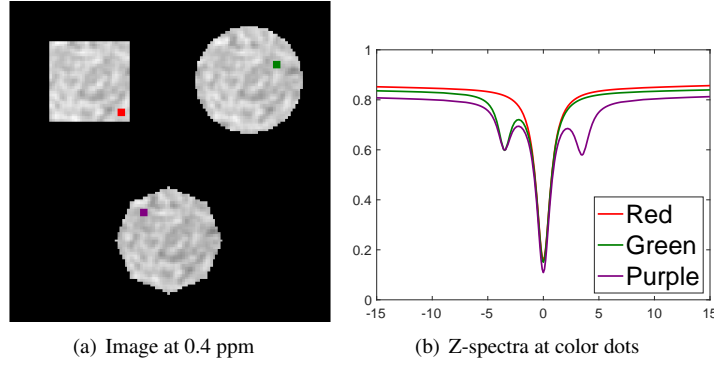


Figure 1: Synthetic phantom visualization.

We simulated three sets of z-spectra by varying the number of basis functions in the Lorentzian model [1, 2] as,

$$L(\Delta\omega) = c - l_{DS}(\Delta\omega) - l_{MT}(\Delta\omega) - l_{APT}(\Delta\omega) - l_{rNOE}(\Delta\omega), \quad (1)$$

where  $c$  is a constant,

$$l_{DS}(\Delta\omega) = \frac{A_{DS}}{1 + (\frac{\Delta\omega - \delta_{DS}}{\Gamma_{DS}/2})^2}, \quad (2)$$

$$l_m(\Delta\omega) = \frac{A_m}{1 + (\frac{\Delta\omega - \delta_{DS} - \delta_m}{\Gamma_m/2})^2}, m \in \{MT, APT, rNOE\}, \quad (3)$$

where  $\Delta\omega$  is chemical shift variable,  $c$  is a constant and  $\delta_{MT} = -2.5ppm$ ,  $\delta_{APT} = 3.5ppm$ ,  $\delta_{rNOE} = -3.5ppm$ .

Parameter settings are shown in Table 1. The square phantom represented the direct water saturation with the MT effect, the circular phantom included extra rNOE effect, and the octagonal phantom added the APT on top of the previous two effects. In addition, we applied Gaussian filtering to the randomly generated parameters in the

Table 1: Range of Randomized Parameters (MIN / MAX).

Phantom	Square	Circle	Octagon
$c$	0.8 / 1	0.8 / 1	0.8 / 1
$\delta_{DS}$	0	0	0
$A_{DS}$	0.6 / 0.8	0.6 / 0.8	0.6 / 0.8
$\Gamma_{DS}$	1 / 2	1 / 2	1 / 2
$A_{MT}$	0.01 / 0.1	0.01 / 0.1	0.01 / 0.1
$\Gamma_{MT}$	80 / 80	80 / 80	80 / 80
$A_{rNOE}$	0	0.1 / 0.3	0.1 / 0.3
$\Gamma_{rNOE}$	-	1 / 2	1 / 2
$A_{APT}$	0	0	0.1 / 0.3
$\Gamma_{APT}$	-	-	1 / 2

Lorentzian model to mimic spatial variance and smoothness, where  $3 \times 3$  Gaussian kernel with  $\sigma = 1$  was used.

## 2 Phantom Denoising Evaluation

### 2.1 Evaluation Metrics Specification

Mean square error (MSE), peak signal-to-noise ratio (PSNR), and structural similarity index (SSIM) were used for data fidelity and image-based quality assessment,

$$\text{MSE} = \sum_{p=1}^{MN} \sum_{q=1}^C (\mathbf{x}_{pq} - \hat{\mathbf{x}}_{pq})^2, \quad (4)$$

$$\text{PSNR} = 10 \cdot \log_{10} \left( \frac{\mathbf{X}_{\max}^2}{\text{MSE}} \right), \quad (5)$$

$$\text{SSIM}(\mathbf{x} - \hat{\mathbf{x}}) = \frac{(2\mu_{\mathbf{x}}\mu_{\hat{\mathbf{x}}} + c_1)(2\sigma_{\mathbf{x}\hat{\mathbf{x}}} + c_2)}{(\mu_{\mathbf{x}}^2 + \mu_{\hat{\mathbf{x}}}^2 + c_1)(\sigma_{\mathbf{x}}^2 + \sigma_{\hat{\mathbf{x}}}^2 + c_2)} \quad (6)$$

where  $\mathbf{x} \in \mathbb{R}^{MN \times C}$  is the noise-free data,  $\hat{\mathbf{x}} \in \mathbb{R}^{MN \times C}$  is the denoised output,  $\mu_{\mathbf{x}}$  and  $\mu_{\hat{\mathbf{x}}}$  are their respective mean values,  $\sigma_{\mathbf{x}}$  and  $\sigma_{\hat{\mathbf{x}}}$  are their respective standard deviations, and  $\sigma_{\mathbf{x}\hat{\mathbf{x}}}$  is their cross-covariance.  $c_1 = 1 \times 10^{-4}$  and  $c_2 = 9 \times 10^{-4}$  are constants to stabilize the division with a weak denominator.

we additionally introduced the natural logarithm of temporal MSE (lnTMSE) to evaluate voxel-wise error,

$$\text{lnTMSE}_p = \ln \sum_{q=1}^C (\mathbf{x}_{pq} - \hat{\mathbf{x}}_{pq})^2, p = 1, \dots, MN. \quad (7)$$

### 2.2 Statistical Results

In this subsection, we elucidate the use of the lnTMSE metric to evaluate the accuracy of signal denoising on a per-signal basis. As an alternative to calculating the error on a

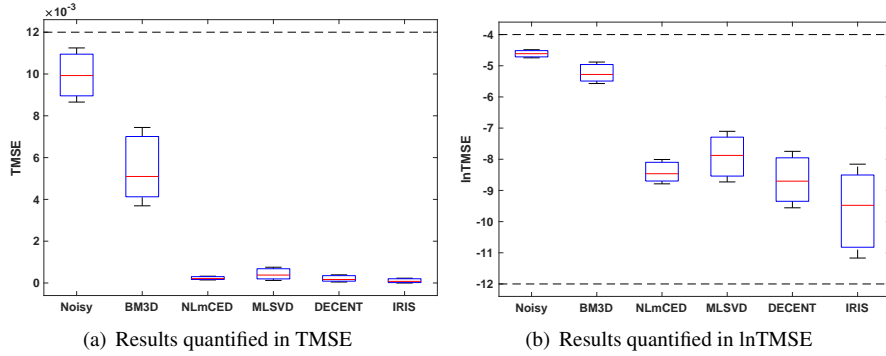


Figure 2: TMSE and lnTMSE shown in boxplots indicates the median and inter-quartile range.

per-voxel basis, we can also employ the TMSE metric,

$$\text{TMSE}_p = \sum_{q=1}^C (\mathbf{x}_{pq} - \hat{\mathbf{x}}_{pq})^2, p = 1, \dots, MN, \quad (8)$$

which does not involve the natural logarithm as in lnTMSE. The results, depicted in Figure 2(a), show that the error distribution of IRIS is closest to zero and exhibits a compact distribution, indicating the absence of “failure samples” in denoising. However, the TMSE values for the noisy and BM3D are relatively larger, narrowing the gap among the results of the last four methods in Figure 2(a). Therefore, we compute the natural logarithm on top of TMSE to magnify the differences near zero for the last four methods, as shown in Figure 2(b). The results demonstrate that the error of IRIS is the smallest, with a considerable portion of the errors even smaller than the minimum achievable error of other methods. However, due to the logarithmic relationship, as the values approach zero, the function exhibits more significant changes, resulting in a less compact distribution when observed from a graphical standpoint. Thus, for the compactness of the distribution, we can only refer to Figure 2(a).

### 3 In-vivo Data Setup

More detailed information about animal subject setup is provided here. For in-vivo evaluation, we have prepared two sets of mice data with tumor: one with minimal noise level (*Clean Subject*) and the other with more noticeable noise (*Noisy Subject*). Both were injected with U-87 MG cell ( $0.5M/3\mu l$ ) at 2.0 mm right-lateral, 0.2 mm anterior and 3.8 mm below the bregma and were anesthetized using 2% isoflurane in a mixture of oxygen (93%) and air gases, and maintained using a bite bar. The body temperature was maintained with a water-heated pad and the respiratory was prudentially monitored for both mice. Before CEST acquisition, the  $B_0$  field over the mouse brain was well adjusted using field-mapping and second-order shimming. The CEST MRI sequence was a continuous-wave (CW) saturation module followed by the rapid acquisition with refocused echoes (RARE) as a readout module. A power (B1) of  $0.8\mu T$  and a duration

Table 2: Boundary and initial value settings (*Clean Subject*) for optimization in Eq. (9).

Conditions	Lower Bound	Upper Bound	Initial Value
$c$	0.9	1	1
$\delta_{DS}$	-0.2	0.2	0
$A_{DS}$	0.5	1	0.8
$\Gamma_{DS}$	1	10	6
$A_{MT}$	0.0025	0.2	0.1
$\Gamma_{MT}$	30	100	200
$A_{rNOE}$	0	0.3	0.1
$\Gamma_{rNOE}$	2	20	8
$A_{APT}$	0	0.4	0.3
$\Gamma_{APT}$	1	8	2

( $t_{sat}$ ) of 3000 ms were used for the saturation module. The saturation frequency varied from  $-15$  to  $15$  ppm, with a  $0.2$  ppm increment and a  $2$  ppm increment between  $-7/7$  and  $-15/15$  ppm. Four M0 images with saturation frequency offset at  $200$  ppm were acquired and averaged for z-spectrum normalization. The readout parameters were as follows: repetition time (TR)=5000 ms, echo time (TE)=5.9 ms, field of view (FOV)= $18 \times 18 mm^2$ , matrix size= $96 \times 96$ , slice thickness=1 mm, RARE factor=32.

## 4 4-pool Lorentzian Fitting

CEST mapping was achieved by 4-pool Lorentzian fitting [2, 3]. The same model in Eq. 1 was applied here for addressing the following non-linear least square problem,

$$\underset{P}{\operatorname{argmin}} \frac{1}{2} \|L_i(P; \Delta\omega) - Z_i(\Delta\omega)\|^2, i = 1, \dots, MN, \quad (9)$$

where  $M \times N$  is the spatial dimension of given data, and  $P$  is the group of parameters in the Lorentzian model being estimated. The optimization problem was solved by “levenberg-marquardt” method signal by signal, of which boundary condition and initial value settings are listed in Table. 2 and Table. 3 for *Clean Subject* and *Noisy Subject* respectively. The optimal  $A_{APT}$  and  $A_{rNOE}$  for each pixel are then formulated to *APT* (3.5ppm) and *rNOE* (-3.5ppm) maps respectively.

## 5 Ablation Study

Apart from the ablation study conducted quantitatively, we further examine the impact on CEST mapping with the selection of  $K$ . A smaller  $K$  will make the denoising method more aggressive but can lead to information loss. Conversely, a larger value of  $K$  will preserve information-related components but may also retain noise. Therefore, an optimal value of  $K$  is needed to balance these two aspects. Figure 3 indicates that APT maps with  $1 \leq K < 4$  exhibit loss of tissue information, while  $K > 4$  results in tumor region showing hypo-intensity. This discrepancy contradicts the expected distribution pattern of APT in tumors. It occurs because when  $K$  is too large, residual noise can introduce significant errors in CEST mapping, similar to the APT maps displayed in

Table 3: Boundary and initial value settings (*Noisy Subject*) for optimization in Eq. (9).

Conditions	Lower Bound	Upper Bound	Initial Value
$c$	0.9	1	1
$\delta_{DS}$	-0.2	0.2	0
$A_{DS}$	0.5	1	0.8
$\Gamma_{DS}$	1	10	6
$A_{MT}$	0.0025	0.2	0.1
$\Gamma_{MT}$	30	100	200
$A_{rNOE}$	0	0.3	0.1
$\Gamma_{rNOE}$	2	20	8
$A_{APT}$	0	0.3	0.1
$\Gamma_{APT}$	1	10	2

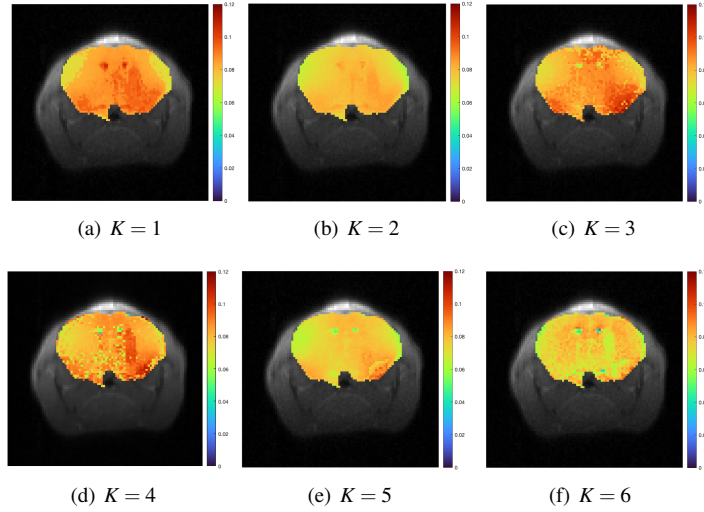


Figure 3: APT (3.5ppm) Map generated from IRIS denoised CEST data regarding to different selection of  $K$ .

the main text of the paper for the *noisy subject* experiment. Other baselines, which did not adequately remove noise, show a similar APT map to the one obtained by IRIS with  $K = 6$  in Figure 3(f), leading to an incorrect APT distribution. Conclusively, the optimal parameter is  $K = 4$ , which aligns with the conclusion drawn in the Ablation Study of the main paper.

## References

- [1] Moritz Zaiss and Peter Bachert. Chemical exchange saturation transfer (cest) and mr z-spectroscopy in vivo: a review of theoretical approaches and methods. *Physics in Medicine & Biology*, 58(22):R221, 2013.
- [2] Steffen Goerke, Yannick Soehngen, Anagha Deshmane, Moritz Zaiss, Johannes Breitling, Philip S Boyd, Kai Herz, Ferdinand Zimmermann, Karel D Klika, Heinz-Peter Schlemmer, et al. Relaxation-compensated apt and rnoe cest-mri of human brain tumors at 3 t. *Magnetic resonance in medicine*, 82(2):622–632, 2019.
- [3] Felix Glang, Anagha Deshmane, Sergey Prokudin, Florian Martin, Kai Herz, Tobias Lindig, Benjamin Bender, Klaus Scheffler, and Moritz Zaiss. Deepcest 3t: Robust mri parameter determination and uncertainty quantification with neural networks—application to cest imaging of the human brain at 3t. *Magnetic Resonance in Medicine*, 84(1):450–466, 2020.